PHYSICAL REVIEW B **66**, 075426 (2002)

Electronic structure and orientation relationship of Li nanoclusters embedded in MgO studied by depth-selective positron annihilation two-dimensional angular correlation

C. V. Falub
Interfaculty Reactor Institute, Delft University of Technology, Mekelweg 15, NL-2629 JB Delft, The Netherlands

P. E. Mijnarends
Interfaculty Reactor Institute, Delft University of Technology, Mekelweg 15, NL-2629 JB Delft, The Netherlands
and Department of Physics, Northeastern University, Boston, Massachusetts 02115

S. W. H. Eijt, M. A. van Huis, A. van Veen, and H. Schut
Interfaculty Reactor Institute, Delft University of Technology, Mekelweg 15, NL-2629 JB Delft, The Netherlands

(Received 26 March 2002; published 30 August 2002)

Quantum-confined positrons are sensitive probes for determining the electronic structure of nanoclusters embedded in materials. In this work, a depth-selective positron annihilation 2D-ACAR (two-dimensional angular correlation of annihilation radiation) method is used to determine the electronic structure of Li nanoclusters formed by implantation of 10^{16}-cm^{-2} 30-keV ^{6}Li ions in MgO (100) and (110) crystals and by subsequent annealing at 950 K. Owing to the difference between the positron affinities of lithium and MgO, the Li nanoclusters act as quantum dots for positrons. 2D-ACAR distributions for different projections reveal a semicoherent fitting of the embedded metallic Li nanoclusters to the host MgO lattice. *Ab initio* Korringa-Kohn-Rostoker calculations of the momentum density show that the anisotropies of the experimental distributions are consistent with an fcc crystal structure of the Li nanoclusters. The observed reduction of the width of the experimental 2D-ACAR distribution is attributed to positron trapping in vacancies associated with Li clusters. This work proposes a method for studying the electronic structure of metallic quantum dots embedded in an insulating material.

DOI: 10.1103/PhysRevB.66.075426 PACS number(s): 61.46.+w, 78.70.Bj, 71.18.+y

I. INTRODUCTION

In view of the current interest in properties of quantum dots, the study of metallic and semiconductor nanoclusters in materials has grown considerably in recent years.[1–3] Owing to their linear and nonlinear optical properties, metallic and semiconductor nanoclusters are of great importance for the field of optoelectronics.[4,5] Nanoclusters embedded in inert matrices are usually produced by ion implantation and subsequent annealing.[6,7] Their size can be influenced by the selection of the type of matrix, the ion implantation fluence and energy, and the time and temperature of the annealing stage. Consequently, one can modify the electronic and optical properties of the matrix in which the nanoclusters are embedded.

The structural properties of nanoclusters are usually characterized by high-resolution x-ray diffraction (XRD) and cross-sectional transmission electron microscopy (XTEM),[8,9] while for a determination of the nanocluster size, optical absorption spectroscopy can also be used.[10,11] However, XTEM requires destruction of the sample while specimen preparation is time consuming. Furthermore, small nanoclusters and nanoclusters of light elements cannot be easily detected with XRD and XTEM techniques. Positrons (e^+) are known to be nondestructive probes of low atomic density regions (e.g., vacancies, vacancy clusters, microcavities) in materials over a wide range of depths, from the surface to depths of hundreds of nanometers.[12] Under favorable conditions of positron affinity, e.g., when the positron affinity of the nanocluster material is lower than that of the host material, positrons can be confined in a nanocluster and upon annihilation provide unique information on the electronic properties of that nanocluster.[13–16] Therefore, depth-selective positron-annihilation spectroscopies are promising techniques for the characterization of nanoclusters produced by ion implantation. Two-dimensional angular correlation of annihilation radiation (2D-ACAR), which measures the angular deviation from collinearity of the coincident photons, offers the advantage of mapping the momentum distribution of the electrons in two dimensions with a high resolution.[17] Therefore, 2D-ACAR yields information regarding the electronic structure of the nanoclusters. One can use either a conventional ^{22}Na e^+ source for bulk studies or a variable energy slow e^+ beam for depth-resolved experiments. However, because of count rate limitations, application of the 2D-ACAR method to depth profiling studies had to wait for the development of high-intensity beams of slow positrons. Nowadays, several high-intensity beams are either operational or under construction.[18] At the Positron Center Delft, a 2D-ACAR setup coupled to the intense ($8\times10^7 e^+$/s) monochromatic slow e^+ beam POSH (pOSitrons from the HOR reactor) is used for depth-selective 2D-ACAR studies on ion implanted and layered materials.[19–21]

In the present paper, Li nanoclusters embedded in monocrystalline MgO are studied by depth-resolved positron annihilation 2D-ACAR spectroscopy. The paper is organized as follows. In Sec. II we give details of the Korringa-Kohn-Rostoker (KKR) momentum density calculations for fcc and bcc Li and for MgO. Section III describes the experimental procedures, while in Sec. IV the results obtained with the

2D-ACAR technique are presented and analyzed in order to extract the orientation relationship of the Li nanoclusters embedded in MgO. To this end three different projections of the 2γ momentum density are considered in order to characterize better the electronic structure of the Li nanoclusters: two for Li implanted MgO(110) and one for Li implanted MgO(100). The results are discussed in Sec. V. Section VI summarizes the conclusions of this work.

II. COMPUTATIONAL DETAILS

The electronic structures of MgO and of bcc and fcc Li were computed using the all-electron self-consistent KKR method.[22–27] The crystal potentials possess the muffin-tin form and are based on the von Barth–Hedin local-density approximation to the exchange-correlation functional.[28] The band structures were solved to a high degree of self-consistency; the bands, Fermi energy, and crystal potential were converged to better than 0.1 mRy. The lattice parameters were 4.212 (MgO), 3.51 (bcc Li), and 4.40 Å (fcc Li), respectively. The positron potential consists of the Hartree term with a minus sign and a positron-electron correlation term given by Boroński and Nieminen.[29] The 2γ momentum density $\rho^{2\gamma}(\mathbf{p}=\mathbf{k}+\mathbf{G})$, given by

$$\rho^{2\gamma}(\mathbf{p})\cong\pi r_0^2 c\sum_j\left|\int d\mathbf{r}e^{-i\mathbf{p}\cdot\mathbf{r}}\psi_j(\mathbf{r})\psi_+(\mathbf{r})\sqrt{\gamma(\mathbf{r})}\right|^2, \tag{2.1}$$

was also evaluated with the aid of the KKR method according to Ref. 30. Here, $\psi_j(\mathbf{r})$ and $\psi_+(\mathbf{r})$ are the electron and positron wave functions, and $\sqrt{\gamma(\mathbf{r})}$ is the enhancement function, which takes into account the formation of a cloud of electrons around the positron owing to electron-positron correlation effects.[29,31] The summation runs over all occupied states *j*. The bands and eigenfunctions are computed at 819 (bcc Li) and 489 (MgO and fcc Li) **k** points in the irreducible 1/48th part of the Brillouin zone. The KKR valence electron wave functions and the positron wave function (the latter at $\mathbf{k}_+=0$) are then transformed into plane-wave representations which are convoluted with one another, using 981 (MgO and fcc Li) or 959 (bcc Li) plane waves for the positron wave function. At every **k** point the momentum density is computed for 1007 (981) **G**'s for the bcc (fcc) structure. In this manner $\rho^{2\gamma}(\mathbf{p})$ was obtained in a sphere of radius 7.85 a.u. (MgO), 7.93 a.u. (bcc Li), or 7.52 a.u. (fcc Li) in **p** space. The various 2D-ACAR distributions $N(p_x,p_y)=\int dp_z\rho^{2\gamma}(\mathbf{p})$ were obtained by projection onto the desired plane.

III. EXPERIMENT

In this work $10\times10\times1$ mm^3 epipolished single crystals of MgO(100) and MgO(110) implanted with (1×10^{16})-cm^{-2} 30-keV ^{6}Li ions and postannealed to 950 K for 30 min were used for the depth-selective positron experiments. The depth-selective 2D-ACAR measurements were carried out using an Anger-camera-type setup coupled with POSH, the high-intensity monoenergetic positron beam with a flux of $8\times10^7 e^+$/s. The slow positrons produced by pair production in a 2MW reactor core are trapped by means of a system of a few electrostatic lenses and magnetically (~0.01 T) guided in vacuum (~10^{-8} mbars) over a distance of ~25 m with a system of long solenoids and Helmholtz coils.[19] Positrons produced at 1.5 keV are accelerated up to about 20 keV in an accelerator stage, positioned ~1 m before the target and consisting of 11 electrostatic lenses. Positron implantation energies lower than 1.5 keV can also be used, but at the expense of a substantial loss of intensity due to the conversion of forward momentum into angular momentum.[32] The beam is focused to a ~3.5-mm-diameter spot at the ACAR target by a 1.37-T NdFeB magnet placed behind the sample.[32] The Anger cameras, used to detect the 511-keV γ radiation stemming from the annihilation of positrons in the sample, consist of 41.8-cm-diameter 1.25-cm-thick NaI crystal scintillators, optically coupled to a close-packed honeycomb array of 61 photomultipliers. A detector-detector distance of ~23 m provides an angular view of ~51×51 mrad^2 (1 mrad is equivalent to 0.137 momentum a.u.) in a 256×256 pixel matrix. A coordinate system (p_x,p_y,p_z) is defined with p_z along the line connecting the cameras and p_y along the positron beam, while p_x lies in the plane of the sample which is mounted perpendicular to p_y. The estimated overall experimental resolution is 1.4×1.1 mrad^2 full width at half maximum (FWHM) for the p_x and p_y directions, respectively. In order to make the resolution the same for both directions we convolute the measured distributions with a Gaussian along the p_y direction. For the MgO(100) single crystal the integration axis p_z is along the [010] direction, while the p_x and p_y directions are parallel to [001] and [100], respectively. For the MgO(110) single crystal, p_z is along [110], while p_x and p_y are parallel to [001] and [110], respectively. In order to perform measurements for the (111) projection, the MgO(110) single crystal is rotated by 35° around the [110] direction (see Fig. 1). Hence, p_z is then along [111], while p_x and p_y are parallel to [112] and [110].

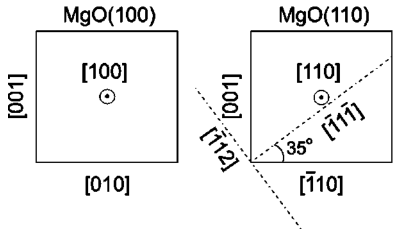

FIG. 1. Sample geometry and crystalline axes of MgO(100) (left) and MgO(110) (right) single crystals.

In view of the insulating properties of MgO, a 15-nm-thick layer of Al was deposited on the sample surface and electrically connected to the sample holder to prevent a buildup of electric charge. In order to select the optimum positron implantation energies for use in the 2D-ACAR experiments the MgO sample was analyzed with Doppler broadening positron beam analysis using both POSH and VEP (a ^{22}Na based slow positron beam).

A 2D-ACAR distribution containing 10.4×10^6 events was collected at a positron implantation energy of 4 keV,

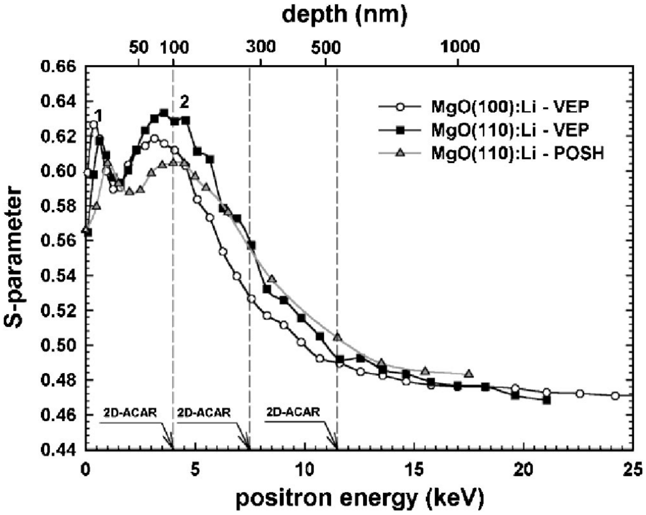

FIG. 2. *S* parameter vs positron implantation energy for Li implanted MgO(100) and MgO(110). Peak 1 corresponds to the Al layer; peak 2 to the Li implantation range.

which corresponds to a mean positron implantation depth coinciding with the center of the Li nanocluster layer, MgO(100):Li. Additionally, 2D-ACAR spectra were collected at 7.5 keV and 11.5 keV, containing 11.5×10^6 and 3.9×10^6 counts, respectively. For comparison, a 2D-ACAR distribution (containing 64.1×10^6 counts) was measured with a conventional ^{22}Na source on an as received sample of MgO(100) in order to obtain the MgO bulk contribution. For the MgO(110) single crystal two measurements (containing 16.9×10^6 and 15.2×10^6 counts) were performed at a positron implantation energy of 4 keV, corresponding to (110) and (111) projections of the momentum density of the annihilation photons, respectively. For comparison, bulk 2D-ACAR spectra (containing 14.7×10^6 and 18.4×10^6 counts, respectively) were measured for the same orientations with the conventional ^{22}Na source. To improve statistics all measured spectra were symmetrized by reflection in the $p_x=0$ and $p_y=0$ mirror planes.

IV. RESULTS

After implantation of monoenergetic ^{6}Li ions in the crystalline MgO matrix and subsequent annealing at 950 K, a layer of Li nanoclusters is formed below the surface.[15] Figure 2 shows the *S* parameter[12] (corresponding to positrons annihilating mostly with valence electrons) versus the positron implantation energy for Li implanted MgO(100) and MgO(110), as obtained from Doppler broadening of annihilation radiation (DBAR) experiments using the VEP and POSH beams. The measured *S* parameter exhibits two peaks: a sharp peak (1) around 0.5 keV corresponding to the 15-nm-thick Al top layer which contains many defects, and a broader one (2) with a maximum around 4 keV, which corresponds to the lithium ion implantation range (about 100 nm) (see Fig. 2). A detailed analysis by means of the fitting code[33]VEPFIT has shown that the *S* parameter curves depicted in Fig. 2 can be fitted very well with a model consisting of five layers:[15] an Al top layer, an intermediate MgO layer, a Li implantation layer (MgO:Li), a layer with the Li implantation tail, and the MgO bulk. This model is consistent with the earlier defect analysis of ion implanted MgO materials that were analyzed with transmission electron microscopy, positron-anihilation spectroscopy, and neutron depth profiling.[10,34,35] In order to obtain more information on the Li implantation layer, three values of the positron implantation energy (E_+) for the 2D-ACAR experiments were selected: 4 keV, 7.5 keV, and 11.5 keV. The energy corresponding to optimum implantation in the lithium layer (MgO:Li) is ≈4 keV if one uses the POSH beam, and about 3.5 keV if one uses the VEP beam. The additional energy of ~0.5 keV is necessary to make up for the transformation of forward momentum into rotational momentum when positrons travel in the nonuniform magnetic field generated by the strong NdFeB focusing magnet.[32]

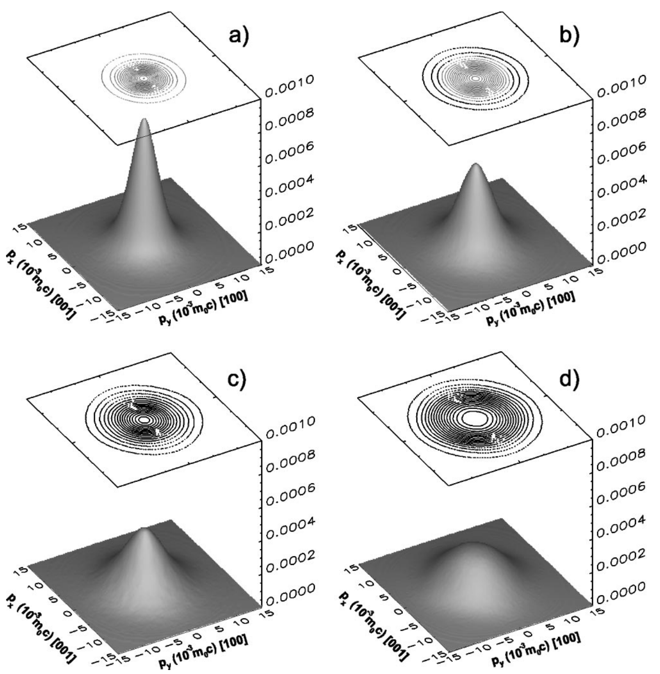

FIG. 3. 2D-ACAR distributions for Li implanted MgO(100) at positron energies of (a) 4 keV, (b) 7.5 keV, and (c) 11.5 keV; (d) 2D-ACAR spectrum for bulk MgO(100). The distributions are normalized to equal total numbers of counts.

Figures 3(a), 3(b), and 3(c) present the 2D-ACAR spectra for the Li implanted MgO(100) sample corresponding to $E_+=4$ keV, 7.5 keV, and 11.5 keV, respectively. For comparison, the bulk spectrum obtained with positrons from a^{22}Na source on an as received MgO(100) single crystal is presented in Fig. 3(d). It is clear that the 4-keV spectrum is much sharper than the bulk spectrum, consistent with the DBAR results, which show a strong increase of the *S* parameter in the Li implantation range. This increase is correlated with the formation of Li nanoclusters in MgO.[15] The 7.5-keV spectrum is still sharp compared to the bulk spectrum, thus showing that at 7.5 keV the contribution of the Li nanoclusters is significant. In the 11.5-keV spectrum this contribution, although weak, is still present, but the spectrum resembles more the bulk spectrum.

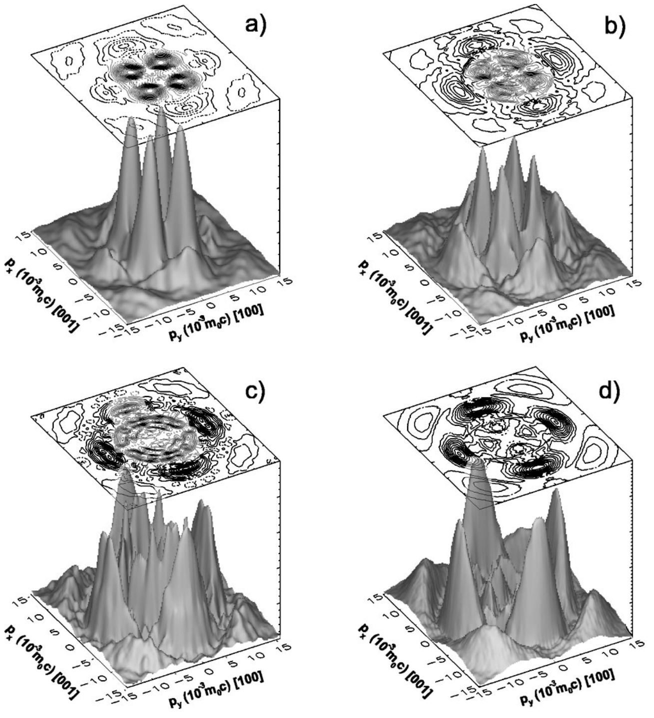

FIG. 4. Anisotropy of the 2D-ACAR distributions in Fig. 3. The distributions are symmetrized and normalized to equal total numbers of counts.

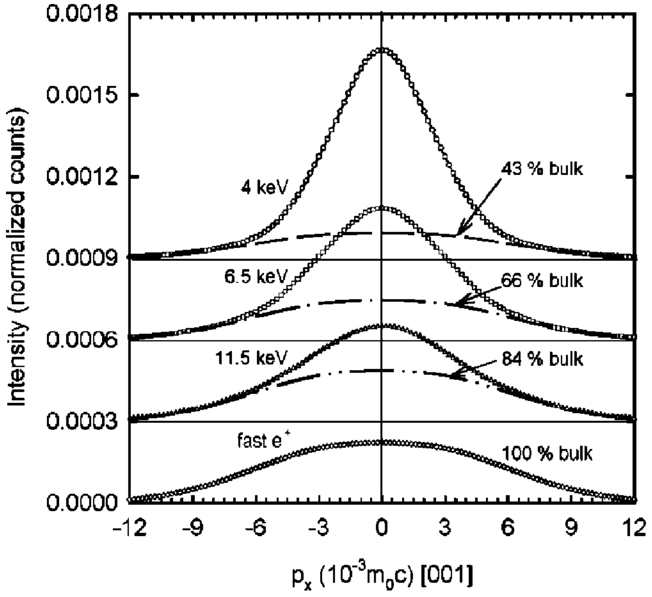

FIG. 5. Cross sections along p_x of the 2D-ACAR distributions for Li implanted MgO at a few positron implantation energies. The cross section of the bulk 2D-ACAR distribution obtained with fast positrons from a ^{22}Na source, and the bulk fractions are also shown. The cross sections are normalized to the total number of counts in the distributions.

Figures 4(a), 4(b), 4(c), and 4(d) show the anisotropy of the 2D-ACAR spectra for 4 keV, 7.5 keV, 11.5 keV, and bulk, respectively. The anisotropic part of each 2D-ACAR spectrum in Fig. 3 was determined by subtracting a radially smoothed isotropic distribution that remains everywhere within the measured spectrum. The anisotropy is therefore everywhere positive. One observes a large difference between the anisotropy of the 4-keV and the bulk distribution. In the 4-keV 2D-ACAR spectrum the bulk MgO(100) anisotropy is still visible, but the main contribution consists of four prominent peaks positioned at a radius of $4.1 \times 10^{-3} m_0 c$, i.e., near the Fermi radius of lithium. Here, m_0 is the electronic rest mass and c is the speed of light. Therefore, one can attribute the anisotropy in the center of Fig. 4(a) to annihilations in the Li nanoclusters, and the fourfold symmetry of this anisotropy suggests that there is an orientation relationship between the Li nanoclusters and the MgO(100) host matrix. In the anisotropy of the 7.5-keV spectrum, shown in Fig. 4(b), the four Li peaks are still present, but they are weaker compared to those found in the 4-keV spectrum. Furthermore, the MgO(100) contribution is enhanced due to the fact that more positrons annihilate with the MgO(100) host electrons. The anisotropy of the 11.5-keV spectrum in Fig. 4(c) closely resembles the MgO(100) bulk spectrum since most of the positrons are implanted in the bulk. The anisotropy of the 11.5-keV spectrum shows a larger contribution of bulk MgO(100), while the peaks attributed to annihilations in Li have a lower intensity than those present in the 4-keV and 7.5-keV spectra. The MgO(100) contributions to the 4-keV, 7.5-keV, and 11.5-keV 2D-ACAR distributions have been determined by subtracting the anisotropy of the bulk spectrum scaled down in order to fit the MgO(100) features. In this manner one finds that in the 4-keV, 7.5-keV, and 11.5-keV distributions, 43%, 66%, and 84% of the annihilations, respectively, take place with the MgO(100) electrons. Furthermore, it is shown in Fig. 5 that the bulk 2D-ACAR spectrum of MgO(100) scaled down to these percentages provides (within ±2%) a good fit to the high-momentum range of the 4-keV, 7.5-keV, and 11.5-keV spectra, respectively.

We have shown that the Li nanoclusters are coherent or semicoherent with the MgO(100) host matrix since the anisotropic contributions displayed in Figs. 4(a) and 4(d) have the same symmetry and identical mirror planes. However, from the above observations alone it cannot be established whether the Li nanoclusters are in the bcc or fcc phase. Treilleux and Chassagne[8,9] found by means of electron diffraction and cross-sectional transmission electron microscopy (XTEM) that, depending on the nanocluster size, metallic lithium can have either the normal bcc or the unusual fcc structure. Furthermore, these authors found the following orientation relationships of the Li nanoclusters in a MgO(100) crystal.

(1) Small Li nanoclusters (less than 15 nm) have the unusual fcc structure and are in simple epitaxy with the matrix: Li (100) ∥ MgO (100) and Li [100] ∥ MgO [100];

(2) Large Li nanoclusters (larger than 35 nm) have a bcc structure which follows the orientation relationship: Li (110) ∥ MgO (111) and Li [111] ∥ MgO [011].

Comparing the experimental settings of the ion implantation and subsequent annealing performed for our samples[15] with those of other works (Refs. 8 and 9), the presence of fcc Li is most likely. We have checked this by calculating the electronic structure of fcc Li in the KKR formalism. How-

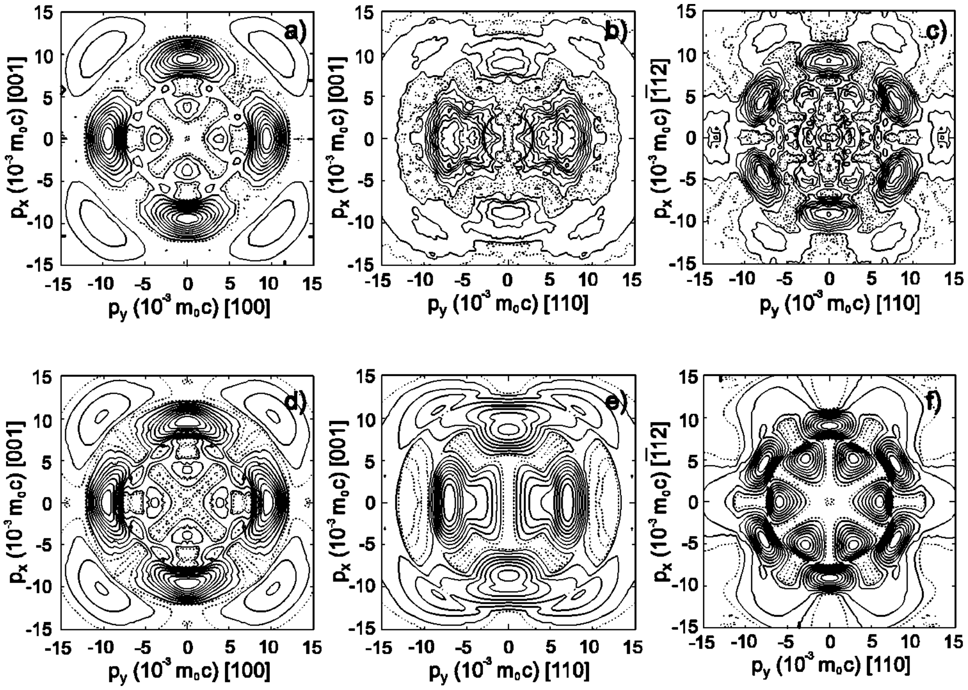

FIG. 6. Anisotropy in the 2D-ACAR distributions of MgO measured with fast positrons, corresponding to the projections along the (a) [010], (b) [110], and (c) [111] directions. Parts (d), (e), and (f) show the corresponding results of KKR theory. The contour interval is 10% (5%) of the peak height for solid (dotted) contours.

ever, before discussing the results of these calculations and comparing them with experiment we show the anisotropy of the 2D-ACAR distributions for nonimplanted MgO as a reference. Figure 6 shows the measured and calculated anisotropy in the 2D-ACAR distributions corresponding to projections along the [010], [110], and [111] directions. There is a good agreement between experiment and theory with respect to the various structure elements in these distributions. The most important difference is found in the [111] projection where theory yields two rings of six peaks each, the peaks in the inner ring having a height of ~75% of those in the second ring. The measurement clearly shows the peaks of the second ring, but the first ring appears to be much weaker than expected, although careful examination of Fig. 6(c) shows a set of weak peaks at the expected positions with a height ~40% of those of the second ring.

Having established nonimplanted MgO as our reference material, Fig. 7 now presents the anisotropy in the 2D-ACAR distributions of Li implanted MgO. The three rows correspond to projections along the [010], [110], and [111] directions. The first two columns show the results of the 4-keV measurements for Li implanted MgO(100) before and after subtraction of the scaled distribution for bulk MgO(100), while the third column shows the calculated anisotropy of fcc Li. Figure 7(a) shows weak features centered at $(p_x,\ p_y)=(\pm 9.5,0)\times 10^{-3} m_0 c$, $(0,\pm 9.5)\times 10^{-3} m_0 c$, and $(\pm 10,\pm 10)\times 10^{-3} m_0 c$. These features are attributed to MgO(100) since they are present in the anisotropy of the bulk MgO(100) spectrum shown in Fig. 6(a). By subtracting the bulk MgO(100) contribution (43%) these features are completely removed [Fig. 7(b)]. Figure 7(c) shows the calculated anisotropy for fcc Li obtained by projecting the 3D-momentum density of Li onto the (100) plane.[36,37] Before subtracting the isotropic distribution, the calculated 2D-ACAR spectrum was convoluted with a two-dimensional Gaussian of 1.4×1.4 $(10^{-3} m_0 c)^2$ FWHM resembling the resolution function of the 2D-ACAR setup. The anisotropy of the calculated spectrum exhibits a fourfold symmetry, and the four prominent peaks in both the theoretical and experimental anisotropy coincide in position. These peaks are located at the projections of the positions where the Fermi surface (FS) touches the hexagonal faces of the first Brillouin zone. Figure 8 presents the band-structure calculation of fcc Li. The relevant feature is the energy difference between the Fermi energy and the energy of the L_1 state: $E_F - E_{L_1} = 1.2$ mRy, equivalent to 16 meV, which implies that the FS displays small necks in the $\langle 111\rangle$ directions. These necks have a diameter of 25% of those in Cu.[38] Because of the subtlety of this feature the potential for fcc Li was converged to better than 10^{-6} Ry. The density of states and the Fermi level were calculated using a fine mesh of 67 626 *ab initio* **k** points in the irreducible 1/48th of the Brillouin zone. The four maxima in the anisotropy are strong since the eight necks of the FS above and below the (100) plane coincide in pairs in projection. In the (200) zones centered at $(p_x, p_y)=(0,\pm 11.5)\times 10^{-3} m_0 c$ and $(\pm 11.5,0)\times 10^{-3} m_0 c$ one discerns in the theoretical anisotropy presented in Fig. 7(c) the weak (200) high-momentum components (HMC) due to umklapp annihilation. The HMC are not visible in the experimental anisotropy, presumably due to their low intensity (of the same order as the background in the 2D-ACAR experiments) and to the overlapping with MgO features.

To gain more insight into the structural properties of the Li nanoclusters, a Li implanted MgO(110) sample has been studied with 2D-ACAR. For this sample, the *S* parameter shows the same trend as for the Li implanted MgO(100) sample, with a sharp peak near the surface attributed to the Al top layer and a broader one with a maximum at 4 keV corresponding to the Li nanoclusters (see Fig. 2). Figure 7(d) presents the anisotropy of the 4-keV 2D-ACAR spectrum for

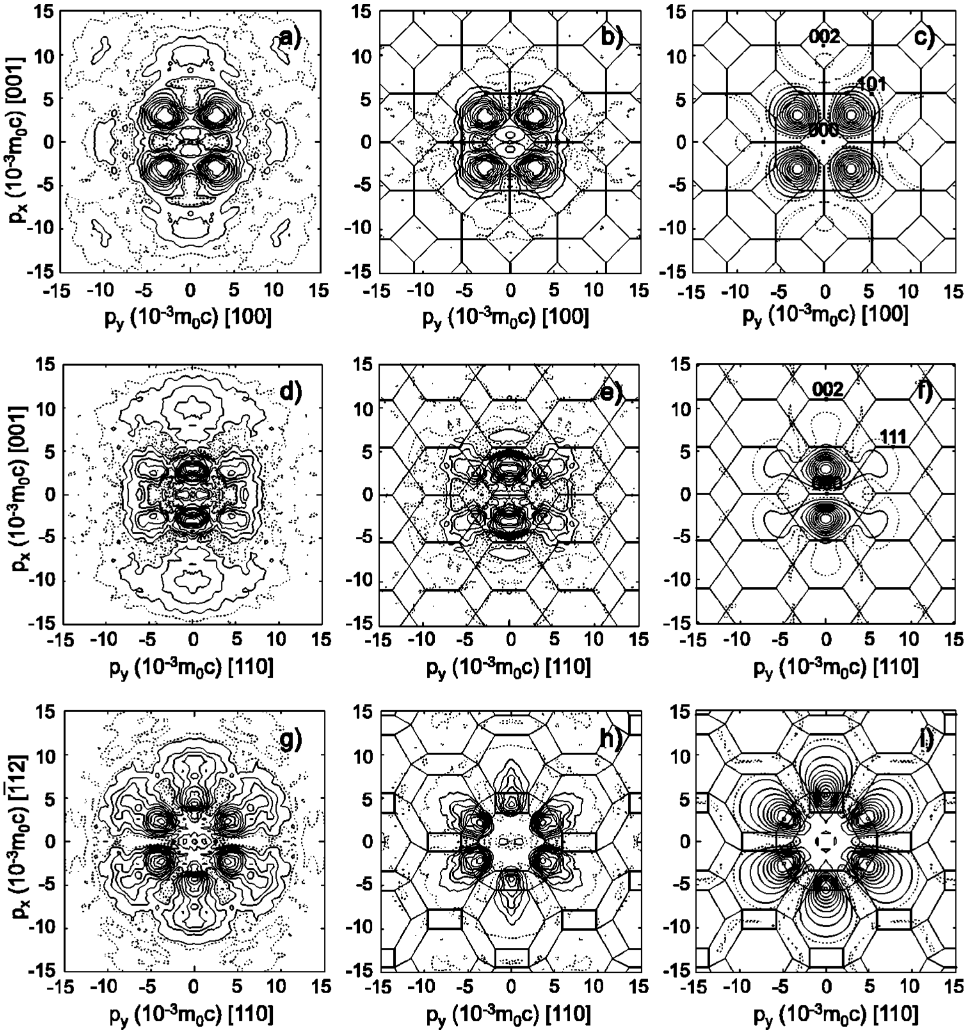

FIG. 7. Anisotropy in the 2D-ACAR distributions. The three rows correspond to projection along the [010], [110], and [111] directions. The first two columns show the symmetrized results of the 4-keV measurements for Li implanted MgO(100) before and after subtraction of the scaled distribution for bulk MgO(100), while the third column shows the calculated anisotropy after convolution with the experimental resolution function. A few reciprocal lattice points are indicated in (c) and (f). The contour interval is 10% (5%) of the peak height for solid (dotted) contours. The solid lines represent the projected Brillouin zones.

Li implanted MgO(110). As in the case of the Li implanted MgO(100) sample, one observes large differences with respect to the anisotropy of the bulk MgO(110), shown in Figs. 6(b) and 6(e). The two peaks centered at $(p_x,p_y)=(\pm 9.5,0)\times 10^{-3}m_0c$ in Fig. 7(d) can be attributed to annihilations with the MgO(110) electrons since they are also observed in the bulk anisotropy shown in Figs. 6(b) and 6(e). Indeed, by subtracting the bulk MgO(110) spectrum, scaled down to 43%, from the 4-keV spectrum, the two peaks along the p_x direction are removed [see Fig. 7(e)]. Figure 7(f) presents the calculated anisotropy of the theoretical fcc Li(110) spectrum obtained by projecting the 3D-momentum density of Li onto the (110) plane. There is a good agreement between the relevant structure elements of the experimental and theoretical anisotropy shown in Figs. 7(e) and 7(f). The two strong peaks, centered at $\pm 3\times 10^{-3}m_0c$ along the p_x direction, are due to the FS touching the hexagonal zone faces above and below the (110) plane. The four weaker peaks correspond to the high-momentum components in the (111) zones, particularly the necks, and are found in both the experimental and theoretical spectra. The necks in the experiment seem to be stronger than in the theory; this may be an effect of enhancement due to positron-electron correlation.[39]

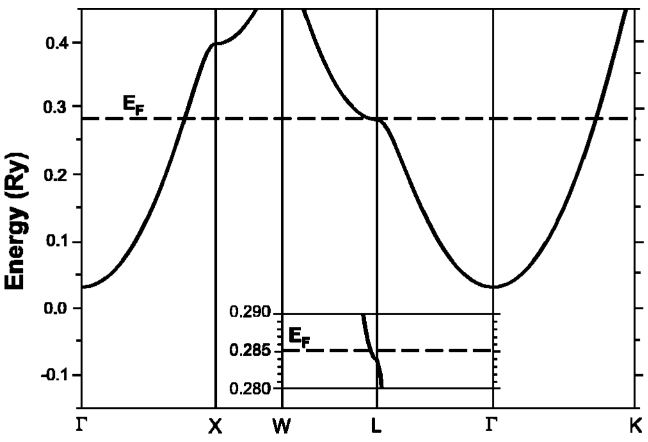

FIG. 8. Band structure of fcc Li. The inset shows the neck at *L* on a magnified energy scale; the horizontal scale is unchanged.

So far, the results for Li implanted MgO(100) and MgO(110) are consistent with Li nanoclusters which have the fcc structure. Additional proof has been obtained by measuring the 2D-ACAR spectrum of Li implanted MgO(110) oriented with the [111] direction along the integration axis of the experiment (p_z). In this situation, the p_x and p_y axes are parallel to the $[\bar{1}12]$ and [110] directions, respectively. Figure 7(g) shows the anisotropy of the 4-keV ⟨111⟩-projected 2D-ACAR spectrum of Li implanted MgO(110). The figure shows six prominent peaks centered at 5.3 $\times 10^{-3} m_0 c$ surrounded by six weaker peaks centered at 9 $\times 10^{-3} m_0 c$, all arranged in a sixfold pattern. Another six peaks, very weak, are present between $10\times 10^{-3} m_0 c$ and $15\times 10^{-3} m_0 c$. Comparing this anisotropy to the anisotropy shown in Fig. 6(c) obtained for the same sample using the 2D-ACAR setup with the fast e^+ source, one can attribute the six prominent peaks to Li and the other 12 peaks to MgO. By subtracting the bulk MgO spectrum, which has been scaled down to 43%, the 12 peaks in the medium- and high-momentum ranges are removed as seen in Fig. 7(h). The bulk MgO fraction of 43% is also obtained by fitting the 4-keV spectrum with the bulk spectrum in the high-momentum range. Figure 7(i) presents the calculated anisotropy of fcc Li(111) after convolution of the theoretical spectrum with the resolution function of the 2D-ACAR setup. This anisotropy closely resembles the experimental anisotropy shown in Fig. 7(h), with small differences consisting of radially somewhat broader theoretical Li peaks that are shifted slightly toward higher momenta.

V. DISCUSSION

Our results show that the metallic Li nanoclusters formed in MgO are in simple epitaxy (cube-on-cube) with the crystalline host matrix. They are consistent with an fcc structure of the Li nanoclusters. In fact, this is expected if one compares our experimental settings for ion implantation with those of Refs. 8 and 9. However, a possible bcc structure of the Li nanoclusters has not yet been excluded. Therefore, we have also performed KKR calculations of the projections of the 3D-momentum density of bcc Li onto the (100), (110), and (111) planes. Figure 9(a) presents the anisotropy of the calculated bcc Li(100) distribution, convoluted with the experimental resolution. One observes the presence of four prominent peaks positioned at $(p_x, p_y) = (\pm 4, \pm 4) \times 10^{-3} m_0 c$. Since the anisotropy of the calculated bcc Li(100) distribution and the experimental anisotropy shown in Fig. 7(b) are different, one can say that if Li nanoclusters with a bcc structure exist in the sample they are not oriented cube-on-cube with the MgO(100) host matrix, in agreement with Refs. 8 and 9. One can also argue that a simple epitaxy of the fcc Li nanoclusters is most likely if one considers the lattice misfits of fcc (4.7%) and bcc (16.6%) Li nanoclusters with the MgO host matrix. A larger misfit between the lattice parameters of the nanoclusters and the host generates a higher surface energy, thereby reducing the probability of formation of these nanoclusters. However, it is clear that the anisotropy of bcc Li(100) could be obtained from the anisotropy of fcc Li(100) by a rotation by 45° [see Fig. 10(b)]. Assuming the presence of bcc Li nanoclusters rotated by 45° (around the [001] axis, as depicted in Figs. 10(b)), then nanoclusters oriented as in Fig. 10(c) and 10(d) should also be present. Figure 9(d) shows the anisotropy of the theoretical spectrum obtained by summing the contributions corresponding to the three configurations presented in Figs. 10(b–d). In this manner, the spectrum contains the bcc Li(100) spectrum rotated over 45°, the bcc Li(110) spectrum, and the bcc Li (110) rotated by 90° around the [001] axis. One observes a striking similarity with the experimental anisotropy shown in Fig. 7(b), and therefore, based only on the 2D-ACAR results, this hypothetical case cannot be excluded. However, the lattice parameter misfit in one of the interfaces is as high as 41%, as seen in Table I. Therefore, the surface energy of the bcc Li nanoclusters embedded in MgO would be significantly higher than in the case of the fcc Li nanoclusters, which are oriented cube-on-cube with the MgO host matrix. Therefore, this particular case can be excluded. Fur-

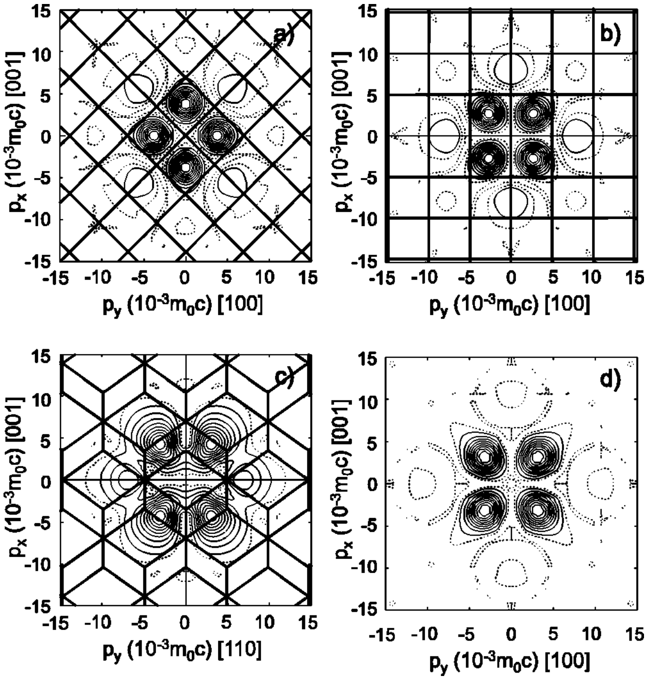

FIG. 9. (a) Anisotropy of the calculated bcc Li(100) distribution; (b) same, rotated by 45°; (c) anisotropy of the calculated bcc Li(110) distribution; (d) anisotropy of the calculated distribution obtained by summing the contributions corresponding to the three configurations presented in Fig. 10.

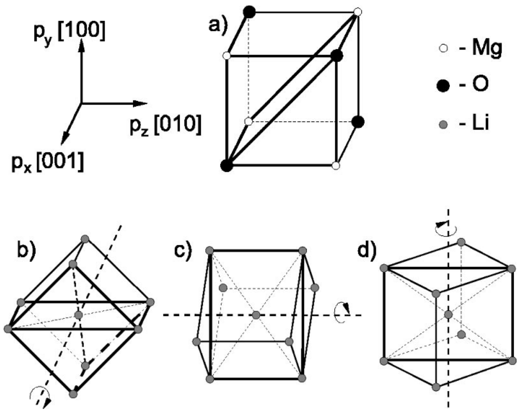

FIG. 10. (a) Unit cell of MgO single crystal; (b)–(d) hypothetical orientations of bcc Li nanoclusters with respect to the MgO host matrix.

TABLE I. Misfit along different directions [*hkl*] (with respect to MgO) at interfaces MgO/bcc-Li.

Interface	MgO(100)/bcc-Li(100)		MgO(110)/bcc-Li(100)	
[*hkl*]	[010]	[001]	[110]	[001]
Misfit (%)	17.8	17.8	16.6	41

thermore, this hypothetical orientation relationship for the bcc Li nanoclusters has not been observed by Treilleux and Chassagne.[8,9]

In order to completely exclude the hypothesis of the bcc Li nanoclusters, one has to examine the orientation relationship for large bcc Li nanoclusters Li (110) ∥ MgO (111) and Li [111] ∥ MgO [011], found in Ref. 8, with the aid of KKR calculations. The authors of Ref. 8 have determined this orientation relationship by performing electron-diffraction experiments on a single precipitate. However, our positron beam has a diameter of about 3 mm FWHM. Therefore, in the presence of bcc Li nanoclusters, the experimental 2D-ACAR spectra should contain information from all bcc Li nanoclusters that are oriented according to the orientation relationship mentioned above or a symmetrically equivalent one. Thus, we want to determine the projection of the momentum distribution of the bcc Li nanoclusters, oriented with respect to the MgO host according to Ref. 8, onto the (100), (110), and (111) planes and to compare the results with the experimental 2D-ACAR spectra. For every MgO (111) plane there are six different but crystallographically equivalent orientations of the Li (110) plane consistent with the orientation condition Li [111] ∥ MgO [011]. Since there are four distinct MgO (111) planes, the final spectrum should contain the contributions of 24 different configurations. However, on closer examination one finds that the six configurations corresponding to one (111) plane are enough to describe the contribution to the spectrum of the bcc Li nanoclusters. The other 18 configurations corresponding to the remaining three planes can be obtained from the first six by symmetry operations, e.g., rotations around the direction of projection. Although we performed the projections for MgO (100), (110), and (111), we present only the results for the (110) case, which shows the largest difference between theory and experiment. Figure 11 shows the anisotropy of the calculated 2D-ACAR spectrum of bcc Li (110) obtained by summing all possible configurations corresponding to the orientation relationship Li (110) ∥ MgO (111) and Li [111] ∥ MgO [011]. The spectrum has been convoluted with the experimental resolution function. The major difference between this anisotropy and the experimental one presented in 7(e) consists in the existence of two strong peaks along the [110] direction in the bcc Li(110) spectrum. Since these peaks do not appear in calculated fcc Li(110) and 4-keV spectra, one can exclude the presence of bcc Li nanoclusters in our sample.

Thus, the Li nanoclusters formed in the studied MgO samples have the fcc structure. This is quite unusual since it is known that Li occurs in nature only as bcc, the fcc phase being only observed at low temperatures and high pressures.[40,41] As mentioned before, the fcc crystal structure of Li has also been observed by Treilleux and Chassagne[8] for small Li nanoclusters (<15 nm). The physical mechanism which induces the small nanoclusters to adopt the fcc structure is not exactly known. For a better understanding of this behavior one should keep in mind that the Li nanoclusters are formed in the ^{6}Li implanted MgO single crystals by annealing up to 950 K followed by a cooling down to room temperature. Hence, during annealing the Li aggregates are formed in the liquid phase and upon cooling they crystallize and form the nanoclusters. Furthermore, it should be pointed out that for small Li nanoclusters the surface plays an important role since a considerable fraction of the Li atoms are located at the periphery of the nanocluster.[42] Therefore, the nanocluster will adopt *that* crystalline phase which minimizes the formation energy of the MgO/Li interface, in other words, one that fits better in the MgO matrix. Since the lattice parameter of fcc Li is closer to that of MgO, the fcc crystalline structure of small Li nanoclusters is more likely. A similar effect was reported in Ref. 13 where the crystal structure of Cu nanoclusters embedded in Fe is expected, on the basis of lattice-parameter similarity, to be bcc rather than fcc.

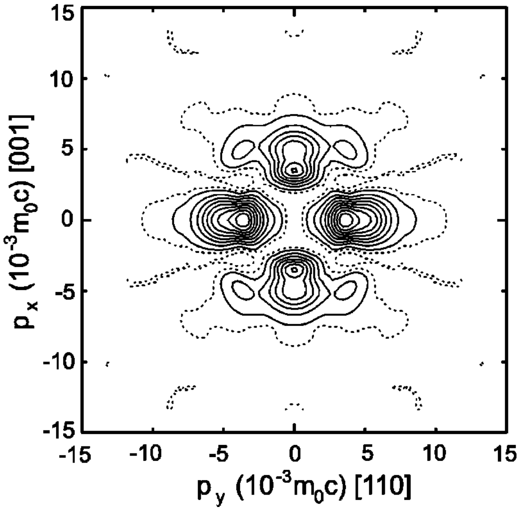

FIG. 11. Anisotropy of the calculated 2D-ACAR spectrum for bcc Li (110) obtained by summing all possible configurations corresponding to the orientation relationship Li (110) ∥ MgO (111) and Li [111]∥ MgO [011].

Another important aspect is the fraction of annihilations in the Li nanoclusters. Our results show that under conditions of optimum implantation in the MgO:Li layer ($E_+ = 4$ keV), 43% of the total number of annihilations is attributed to MgO electrons. Owing to the broad implantation profile, this fraction includes annihilations from adjacent layers. VEPFIT fraction analysis of the Doppler broadening experiments shows that 63% of the 4-keV positrons annihilate in the MgO:Li layer and that 37% of the 4-keV positrons annihilate in MgO above or below this layer. Therefore, the fraction of positrons annihilating with the MgO electrons in the MgO:Li layer is only (43−37)/63=10%, while ∼90% annihilates in lithium nanoclusters. This indicates a high efficiency of positron confinement in Li nanoclusters due to the different positron affinities of MgO and Li.[15]

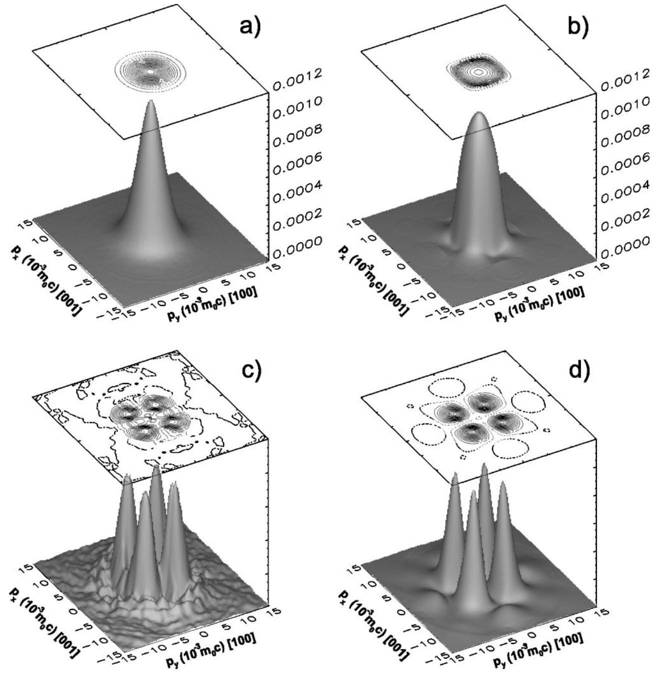

FIG. 12. (a) Experimental 2D-ACAR distribution after subtracting the bulk MgO(100) contribution (43%); (b) theoretical spectrum of fcc Li(100); (c) and (d) anisotropies of the distributions in (a) and (b). The distributions are normalized with respect to the total number of counts.

However, the question arises whether the remaining 57% of annihilations in the 4-keV spectrum can be attributed entirely to trapping in Li nanoclusters, or whether other phenomena [e.g., annihilation of positronium (Ps) atoms, annihilation of positrons at the MgO/Li interface, annihilation of positrons in Li vacancies] contribute to the distribution.

Figure 12 compares the experimental distribution with the results of the KKR computation. The reason to compare the experimental spectrum of Li implanted MgO with the theoretical spectrum of fcc Li is based on the fact that Li is present in nature only as bcc and to our knowledge there are no available 2D-ACAR data on fcc Li. Figure 12(a) shows the experimental spectrum after subtraction of the bulk MgO(100) contribution (43%). Figure 12(b) presents the theoretical spectrum for the valence electrons of fcc Li(100) obtained using the KKR formalism.[43] These distributions exhibit a very similar anisotropy, as shown in Figs. 12(c) and 12(d). The height of the peaks in the calculated anisotropy is 12% of the height of the calculated 2D-ACAR distribution without the core (see below), but the anisotropy of the experimental spectrum is much weaker (2%), which is reflected in a smoother 2D-ACAR spectrum. Also, the experimental distribution is more pointed than the computed one. One can estimate the fraction of annihilations with bulk fcc Li(100) by looking at the difference in height of the peaks in the experimental and theoretical anisotropy. Figure 13 shows that ~21% of the remaining spectrum after subtracting the bulk MgO(100) contribution (43%) can be attributed to annihilations with bulk fcc Li(100). This brings the fraction of bulk fcc Li(100) in the 4-keV spectrum to 12%. However, this percentage was determined by comparing the experimental and theoretical anisotropy and, moreover, the *ab initio* calculations were performed in the independent-particle model (IPM) approximation, e.g., without enhancement. Enhancement is known to affect the shape of the 2D-ACAR profile.[44] Furthermore, core annihilation, which contributes a broad background, is also not taken into account. Thus, the determined fraction of 12% from the 4-keV spectrum attributed to bulk fcc Li(100) should be taken with reserve. However, this suggests that besides the bulk MgO(100) and fcc Li(100) contributions a significant part of the 4-keV spectrum is caused by annihilation processes that have not been taken into account.

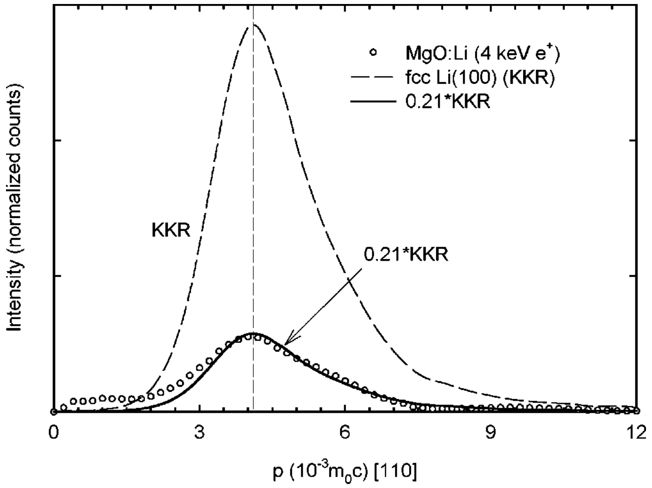

FIG. 13. Cross sections of the experimental [4-keV MgO(100):Li] and theoretical [fcc Li(100)] anisotropy along the [110] direction.

van Huis *et al.*[15] show on the basis of calculations of the positron affinity of MgO and Li that a positron reaching the MgO/Li interface is confined in the Li nanocluster. Therefore, positron trapping at a pure MgO/Li interface is not likely to happen. Furthermore, according to Refs. 15 and 45, annihilation of Ps atoms in cavities is also not likely, since after annealing of the MgO samples at 950 K, the MgO vacancies responsible for the formation of cavities disappear. However, larger cavities can survive this temperature, but they are not observed by XTEM.[46]

We present three possible causes that could explain the difference between the shapes of the calculated and experimental spectra.

(a) *Positron trapping in vacancies and vacancy clusters present in the Li nanoclusters*. A possible reason for the narrowing of the 4-keV spectrum could be positron trapping in different kinds of Li vacancies present in the nanoclusters. At room temperature, which is at already about 2/3 of the bulk Li melting temperature ($T_m = 453.7$ K), a considerable concentration of Li vacancies can be expected. It is known that annihilation of positrons in vacancy-type defects results in a sharper momentum distribution. The presence of vacancies is also suggested by the absence of the HMC in the experimental distributions (see Fig. 12). Positron-annihilation 2D-ACAR studies in aluminum[47,48] show a large increase of the ACAR peak height with increasing temperature. Those studies show that at 613 K, i.e., about 2/3 of the melting temperature of Al ($T_m = 933.5$ K), the ACAR distribution is sharper by ~20% in FWHM than the ACAR at 293 K because of annihilations of positrons trapped in thermally generated monovacancies and divacancies. Furthermore, the shape and linewidth narrowing (~22% lower FWHM) obtained in the present study are comparable. Moreover, both in the present case and in that of vacancy related annihilation in Al it was found that the anisotropy of the ACAR spectra is weak. Therefore, based on these observations, one cannot exclude annihilation of positrons at Li vacancies in the nanoclusters in our case. It should, however, be noted that the binding energy of a positron in a Li monovacancy is too low to cause trapping.[49–51] Neither positron lifetime nor 1D-ACAR measurements in the alkali metals have indicated evidence of trapping by vacancies.[52,53]

Future investigations including measurements at low temperature to reduce the thermal generation of vacancies are necessary to accurately quantify the fraction of annihilations in Li vacancies and to identify the type of vacancies. At present, we do not have the means to perform depth-selective 2D-ACAR experiments at low temperature, but we plan to extend our facility in this direction.

(b) *Positron trapping in interface defects*. Positron trapping in defects (e.g., vacancies or vacancy clusters) located at the MgO/Li interface could contribute to the 4-keV spectrum. These defects can be formed as a consequence of the relative thermal contraction of the Li nanoclusters with respect to the surrounding MgO matrix during cooling from 950 K to room temperature.[54] It is not exactly known how a positron behaves when it is trapped in such an interface defect. However, the wave function of the trapped positron would not significantly probe the bulk MgO since otherwise a larger contribution from MgO, would be found in the spectrum. Thus, positrons trapped in defects at the MgO/Li interface would rather carry the signature of defects and Li atoms at the periphery of the nanocluster than the signature of MgO. As a corollary of this, a small part of the observed fcc Li anisotropy may stem from positrons annihilating in interface defects.

(c) *Calculations*. Since our calculations were performed in the IPM formalism and the core electrons were not taken into account, the theoretical 2D-ACAR distributions can be somewhat different from the experimental ones. The neglect of enhancement and core annihilation alone, however, cannot explain the considerable narrowing of the experimental distribution. A more serious limitation of the calculations is the approximation of the small nanoclusters by an infinite Li crystal, since the contribution of the interface energy of these nanoclusters is significant. Confinement of electrons and positron in small nanoclusters will also affect the width of the 2D-ACAR distribution.

VI. CONCLUSIONS

In this work, Li nanoclusters embedded in MgO(100) and MgO(110) single crystals by low-dose ^{6}Li ion implantation have been studied with a 2D-ACAR setup coupled to the high-intensity monoenergetic slow positron beam POSH. The anisotropic contribution of the 4-keV 2D-ACAR spectrum, corresponding to optimum implantation in the layer containing the Li nanoclusters, exhibits the same fourfold symmetry and mirror planes as the crystalline MgO host matrix. This proves that the Li nanoclusters are semicoherent with the MgO host matrix. The anisotropy of the measured 2D-ACAR distributions in our samples agrees well with *ab initio* calculations of the anisotropy for bulk fcc Li. A simple epitaxy of bcc nanoclusters is excluded, as is the more complicated orientation relationship found by Treilleux and Chassagne for large Li nanoclusters. In order to explain the narrowing of the experimental distributions with respect to those calculated, different scenarios have been proposed. The most likely are trapping of positrons at defects located at the MgO/fcc-Li interface. It has also been pointed out that the *ab initio* calculations have limitations, e.g., they were performed on perfect crystals of infinite size. Therefore, they should be extended to include small Li nanoclusters embedded in MgO.

ACKNOWLEDGMENTS

We would like to thank A. Bansil and B. Barbiellini for useful discussions. This work was sponsored by the Stichting Nationale Computer Faciliteiten for the use of supercomputer facilities, with financial support from the Netherlands Organization for Scientific Research (NWO), and benefited from the allocation of supercomputer time at the Northeastern University Advanced Scientific Computation Center (NU-ASCC).

---

[1] *Metal Clusters*, edited by W. Ekardt (Wiley, New York, 1999).

[2] *Semiconductor Nanoclusters*, edited by P.V. Kamat and D. Meisel (Elsevier, Amsterdam, 1997).

[3] D. Davidovic and M. Tinkham, Phys. Rev. Lett. **83**, 1644 (1999).

[4] P. Chakraborty, J. Mater. Sci. **33**, 2235 (1998).

[5] K. Fukumi, A. Chayahara, K. Kodano, T. Sakaguchi, Y. Horino, M. Miya, K. Jujii, J. Hayakawa, and M. Satou, J. Appl. Phys. **75**, 3075 (1994).

[6] C.W. White, J.D. Budai, S.P. Withrow, J.G. Zhu, E. Sonder, R.A. Zuhr, A. Meldrum, D.M. Hembree, Jr., D.O. Henderson, and S. Prawer, Nucl. Instrum. Methods Phys. Res. B **141**, 228 (1998).

[7] R.L. Zimmerman, D. Ila, E.K. Williams, D.B. Poker, D.K. Hensley, C. Klatt, and S. Kalbitzer, Nucl. Instrum. Methods Phys. Res. B **148**, 1064 (1999).

[8] M. Treilleux and G. Chassagne, J. Phys. (Paris) **40**, L-283 (1979).

[9] M. Treilleux and G. Chassagne, J. Phys. (Paris), Colloq. **41C-6**, C6/391 (1980).

[10] M.A. van Huis, A.V. Fedorov, A. van Veen, F. Labohm, H. Schut, P.E. Mijnarends, B.J. Kooi, and J.Th.M. De Hosson, Mater. Sci. Forum **363–365**, 448 (2001).

[11] M.A. van Huis, A.V. Fedorov, A. van Veen, C.V. Falub, S.W.H. Eijt, B.J. Kooi, J.Th.M. De Hosson, T. Hibma, and R.L. Zim-

merman, Nucl. Instrum. Methods Phys. Res. B **191**, 442 (2002).

[12] P.J. Schultz and K.G. Lynn, Rev. Mod. Phys. **60**, 701 (1988).

[13] Y. Nagai, M. Hasegawa, Z. Tang, A. Hempel, K. Yubuta, T. Shimamura, Y. Kawazoe, A. Kawai, and F. Kano, Phys. Rev. B **61**, 6574 (2000).

[14] Y. Nagai, T. Chiba, Z. Tang, T. Akahane, T. Kanai, M. Hasegawa, M. Takenaka, and E. Kuramoto, Phys. Rev. Lett. **87**, 176402 (2001).

[15] M.A. van Huis, A. van Veen, H. Schut, C.V. Falub, S.W.H. Eijt, P.E. Mijnarends, and J. Kuriplach, Phys. Rev. B **65**, 085416 (2002).

[16] C.V. Falub, P.E. Mijnarends, S.W.H. Eijt, A. van Veen, and H. Schut, Nucl. Instrum. Methods Phys. Res. B **191**, 275 (2002).

[17] R.N. West, in *Positron Spectroscopy of Solids*, edited by A. Dupasquier and A.P. Mills, Jr. (North-Holland, Amsterdam, 1995), p. 75.

[18] R.H. Howell, in *Positron Beams and their Applications*, edited by P.G. Coleman (World Scientific, Singapore, 2000), p. 307.

[19] A. van Veen, H. Schut, J. de Roode, F. Labohm, C.V. Falub, S.W.H. Eijt, and P.E. Mijnarends, Mater. Sci. Forum **363–365**, 415 (2001).

[20] C.V. Falub, S.W.H. Eijt, A. van Veen, P.E. Mijnarends, and H. Schut, Mater. Sci. Forum **363–365**, 561 (2001).

[21] H. Schut, A. van Veen, C.V. Falub, J. de Roode, and F. Labohm, Mater. Sci. Forum **363–365**, 430 (2001).

[22] J. Korringa, Physica (Utrecht) **13**, 392 (1947); W. Kohn and N. Rostoker, Phys. Rev. **94**, 1111 (1954).

[23] S. Kaprzyk and A. Bansil, Phys. Rev. B **42**, 7358 (1990).

[24] A. Bansil and S. Kaprzyk, Phys. Rev. B **43**, 10 335 (1991).

[25] A. Bansil, S. Kaprzyk, and J. Tobo*ł*a, in *Applications of Multiple Scattering Theory to Materials Science*, edited by W.H. Butler, P.H. Dederichs, A. Gonis, and R. Weaver, MRS Symposia Proceedings No. **253** (Materials Research Society, Pittsburgh, 1992), p. 505.

[26] S. Kaprzyk, Acta Phys. Pol. A **91**, 135 (1997).

[27] A. Bansil, S. Kaprzyk, P.E. Mijnarends, and J. Tobo*ł*a, Phys. Rev. B **60**, 13 396 (1999).

[28] U. von Barth and L. Hedin, J. Phys. C **5**, 1629 (1972); A.K. Rajagopal and J. Callaway, Phys. Rev. B **7**, 1912 (1973).

[29] E. Boroński and R.M. Nieminen, Phys. Rev. B **34**, 3820 (1986).

[30] P. E. Mijnarends and A. Bansil, in *Positron Spectroscopy of Solids*, edited by A. Dupasquier and A. P. Mills, Jr. (IOS, Amsterdam, 1995), p. 25.

[31] In our calculations we have set $\gamma(\mathbf{r})=1$ since the enhancement hardly affects the anisotropy of the momentum density, which is our main object of interest in this work.

[32] C.V. Falub, S.W.H. Eijt, P.E. Mijnarends, H. Schut, and A. van Veen, Nucl. Instrum. Methods Phys. Res. A **488/3**, 478 (2002).

[33] A. van Veen, H. Schut, J. de Vries, R.A. Hakvoort, and M.R. Ijpma, in *Positron Beams for Solids and Surfaces*, edited by P.J. Schultz, G.R. Massoumi, and P.J. Simpson, AIP Conf. Proc. **218** (AIP, New York, 1990), p. 171.

[34] A. van Veen, M.A. van Huis, A.V. Fedorov, H. Schut, C.V. Falub, S.W.H. Eijt, F. Labohm, B.J. Kooi, and J.Th.M. DeHosson, in *Ion Beam Synthesis and Processing Materials*, edited by S.C. Moss, K.-H. Heinig, and D.B. Poker, MRS Symposia Proceedings No. 647 (Materials Research Society, Pittsburgh, 2001), p. 011.24.

[35] B.J. Kooi, A. van Veen, J.Th.M. de Hosson, H. Schut, A.V. Fedorov, and F. Labohm, Appl. Phys. Lett. **76**, 1110 (2000).

[36] In computing the anisotropy, the theoretical distributions were subjected to the same procedures of analysis as the experimental spectra.

[37] In the following we mean by (*hkl*) the (*hkl*) plane and all crystallographically equivalent planes.

[38] M.R. Halse, Philos. Trans. R. Soc. London, Ser. A **265**, 507 (1969).

[39] S. Wakoh, S. Berko, M. Haghgooie, and J.J. Mader, J. Phys. F: Met. Phys. **9**, L-231 (1979).

[40] N.E. Christensen and D.L. Novikov, Phys. Rev. Lett. **86**, 1861 (2001).

[41] V.G. Vaks, M.I. Katsnelson, V.G. Koreshkov, A.I. Likhtenstein, O.E. Parfenov, V.F. Skok, V.A. Sukhoparov, A.V. Trefilov, and A.A. Chernyshov, J. Phys.: Condens. Matter **1**, 5319 (1989).

[42] A Li nanocluster with a size of 1.0 nm has ~70% of the atoms at the periphery.

[43] The core electrons yield a weak, broad, and essentially isotropic contribution to the spectrum, which has not been included in the calculation.

[44] L. Oberli, A.A. Manuel, R. Sachot, P. Descouts, and M. Peter, Phys. Rev. B **31**, 6104 (1984).

[45] A. van Veen, M.A. van Huis, A.V. Fedorov, H. Schut, F. Labohm, B.J. Kooi, and J.Th.M. De Hosson, Nucl. Instrum. Methods Phys. Res. B **191**, 610 (2002).

[46] Cavities in MgO are only observed when heavy ions (Au, Ag, etc.) are used with a sufficiently high dose, or for the specific case of noble gas He ions.

[47] M.J. Fluss, S. Berko, B. Chakraborty, K.R. Hoffmann, P. Lippel, and R. W Siegel, J. Phys. F: Met. Phys. **14**, 2831 (1984).

[48] M.J. Fluss, S. Berko, B. Chakraborty, P. Lippel, and R. W Siegel, J. Phys. F: Met. Phys. **14**, 2855 (1984).

[49] C.H. Hodges, Phys. Rev. Lett. **25**, 284 (1970).

[50] M. Manninen, R. Nieminen, and P. Hautojärvi, Phys. Rev. B **12**, 4012 (1975).

[51] R.M. Nieminen and M.J. Manninen, in *Positrons in Solids*, edited by P. Hautojärvi (Springer-Verlag, Berlin, 1979), p. 145.

[52] I.K. MacKenzie, T.W. Craig, and B.T.A. McKee, Phys. Lett. **36A**, 227 (1971).

[53] S.M. Kim and A.T. Stewart, Phys. Rev. B **11**, 2490 (1975).

[54] Taking into account the significant difference between the coefficients of thermal expansion for Li (liquid and solid phases) and MgO (solid phase)—and ignoring relaxation—we have estimated that for a Li nanocluster with a radius of 1 nm, ~20 Li vacancies are formed at the periphery of the nanocluster during cooling from 950 K to room temperature.